Metrology of thin transparent optics using Shack-Hartmann wavefront sensing

Craig R. Forest
Claude R. Canizares
Massachusetts Institute of Technology
Center for Space Research
Cambridge, Massachusetts 02139

Daniel R. Neal
WaveFront Sciences, Incorporated
14810 Central Southeast
Albuquerque, New Mexico 87123

Michael McGuirk, MEMBER SPIE
Mark L. Schattenburg, MEMBER SPIE
Massachusetts Institute of Technology
Center for Space Research
Cambridge, Massachusetts 02139

Abstract. The surface topography of thin, transparent materials is of interest in many areas. Some examples include glass substrates for computer hard disks, photomasks in the semiconductor industry, flat panel displays, and x-ray telescope optics. Some of these applications require individual foils to be manufactured with figure errors that are a small fraction of a micron over 10- to 200-mm lengths. Accurate surface metrology is essential to confirm the efficacy of manufacturing and substrate flattening processes. Assembly of these floppy optics is also facilitated by such a metrology tool. We report on the design and performance of a novel deep-ultraviolet (deep-UV) Shack-Hartmann surface metrology tool developed for this purpose. The use of deep-UV wavelengths is particularly advantageous for studying transparent substrates such as glass, which are virtually opaque to wavelengths below 260 nm. The system has a $143 \times 143\text{-mm}^2$ field of view at the object plane. Performance specifications include 350-μrad angular dynamic range and 0.5-μrad angular sensitivity. Surface maps over a 100 mm diam are accurate to <17-nm rms and repeatable to 5 nm rms. © *2004 Society of Photo-Optical Instrumentation Engineers.* [DOI: 10.1117/1.1645256]

1 Introduction

Metrology is essential for successfully shaping foil optics. Metrological feedback closes the loop on the manufacturing process. Quantifying figure errors permits the evaluation of process improvements. During assembly, micron level distortions to the foil optic may occur due to gravity or friction. Material thermal expansion mismatch may also cause low spatial frequency distortion. Study of these effects requires a metrology tool with a large viewing area, high angular resolution, and large angular range.

One application for x-ray telescope foil optics requires the accurate shaping, patterning, and assembly of thousands of thin, flat grating substrates.[1] Depending on the particular grating geometry, grating substrates are generally rectangular with dimensions on the order of 140 mm and thickness ranging from 0.4 to 2 mm. A variety of substrate materials have been proposed, including borosilicate glass, silicon, and silicon carbide. The foil specifications include a flatness of 500 nm over the surface of the optic, thickness variation of 20 μm over the length, and surface roughness tolerance of <0.5 nm. These foil size specifications are driven by the telescope weight budget and assembly technology. Flatness and surface roughness requirements are driven by resolution goals. Here, when we use the term "flatness," we mean the shape of the front surface of the optic, and not the thickness variation, which is widely misused.

There are three principle functional requirements for this non-null aspheric metrology system, as described by Greivenkamp et al.[2]:

- the system must be able to measure the observable output with sufficient angular dynamic range and precision (angular resolution) to record the large amount of asphericity that is present
- the optic system used to create the observable output must be designed so that no vignetting of the aspheric wavefront occurs
- the system must be calibrated to relate the details in the observable output to the surface under test.

The factory-supplied stock optic foils for our shaping processes typically have low spatial frequency distortions, as observed with other metrology tools. (Interferometric maps and Hartmann tests reveal about three waves per optic length of 100 mm.) Stock borosilicate glass sheets (Schott Glas, model D-263) have large distortions, up to 600 μm over their 100-mm lengths for 400-μm-thick foils. By comparison, silicon wafers typically have a flatness of 3 μm over a 10-mm lateral distance, or 0.3 mrad. We specify 0.3 mrad as the angular range functional requirement for the metrology tool. We seek to flatten these materials to <0.5 μm peak-to-valley (PV) over one 100-mm-diam face. This corresponds to a measurement angular sensitivity

of 50 μrad over a 10-mm lateral distance. We desire a sensitivity that is five times better than the allowable, so the angular sensitivity functional requirement becomes 10 μrad.

1.1 Metrology Technology Candidates: Research Review

Demand for metrology of thin, transparent materials has resulted in many solutions to the problem. Here we present technical details of related work and discuss their relative merits and drawbacks.

A key challenge for optical techniques is the measurement of the front surface of the object without the effect of the reflection from the rear surface. We consider phase shifting interferometry (PSI) methods using short coherence length sources in various configurations,[3–7] mathematically deconvolving the contributions of the two reflections using wavelength tunable sources[8,9] with some mathematical manipulation,[10,11] spatial separation of the two reflections,[12,13] grating interferometers,[14,15] and use of a diode source and optical path difference (OPD) that is a multiple of the laser cavity length.[16] We also consider mechanical methods, such as coatings and contact probes. Lastly, the Shack-Hartmann technique is presented.

1.1.1 Rear- and front-surface coatings

One method for frustrating rear-surface reflection is the application of an appropriate index-matching coating. One may also apply a highly reflective coating to the front surface, thereby eliminating the back reflection. Unfortunately, this impairs routine inspection of optic foils by adding complex application and cleaning procedures. In our case, coatings induce warp on the thin optics or change their elastic behavior as well as require subsequent cleaning.[17]

1.1.2 Partially coherent or white-light illumination for phase shifting interferometry

White light has a much shorter coherence length than a monochromatic laser, owing to the range of wavelengths that comprise it. This has been exploited in modern interferometry to eliminate ghost fringes from the back reflection of a transparent material, among other applications.[18] This technique is limited to samples whose warp is less than their thickness.

A Michelson interferometer has been commonly used for white-light interferometry. In this setup, unwanted interference fringe patterns from parallel surfaces of transmissive plates are eliminated by limiting the production of interference fringe patterns to reference and test surfaces located at equal optical path lengths along reference and test arms. More precisely, the lengths of both arms are carefully adjusted, such that the optical path difference (OPD) is within the source's coherence length.[5–7] Well-matched optics are required between the reference and test arms, which can be prohibitively expensive for measuring large test plates. ADE Phase Shift (Tucson, Arizona) has developed an equal path interferometer for this purpose.[3] This instrument features a 2- to 3-μm coherence length. The front or rear face of photomasks and flat panel displays, which are thicker than this, can be successfully measured, since interference fringes will only be formed from one surface.

A white-light Fizeau interferometer reported by Schwider[4] achieved similar results. Schwider combined a Fabry-Perot interferometer in front of a two-beam Fizeau interferometer to obtain white-light fringes. One disadvantage to this setup is the poor light efficiency caused by the low reflectance of the Fizeau plates, and the low transparency of the Fabry-Perot interferometer averaged over the full-width half maximum (FWHM) of the interference filter.

1.1.3 Wavelength-tuned phase shifting interferometry

de Groot, Smythe, and Deck[10,11] have developed a Fizeau interferometer operating with software that mathematically separates the interference contributions of plane-parallel surfaces. This solution is based on processing the interference data generated with two single-mode wavelengths. The cumulative interference produced by three surfaces R, T, and S (reference, test, and rear) is measured with a first wavelength λ_1 and then with a second wavelength λ_2, in sequence. The sample is then flipped over with the rear surface S now facing the reference surface R, and the cumulative interference is again measured with the two wavelengths λ_1 and λ_2. Thus, four sets of data are generated from which the desired interference between the reference and the test beams may be extracted by mathematical manipulation. The measurement of either or both parallel surfaces of a test plate therefore requires a sequence of phase shift measurements and inversion of the test plate for measuring both surfaces in two opposite orientations. This method requires double handling of the sample, which should be avoided with our low stiffness foils.

A Twyman-Green interferometer has been developed by Okada et al.[8,9] that can obtain separate measurements of surface shapes and refractive index inhomogeneity of optical elements using tunable-source phase shifting interferometry. Separation of the interferogram from the front and rear surface becomes possible, since the wavelength change is proportional to the OPD of the two arms (reference and test). This means that interferograms with different optical path differences have a different amount of phase shift. This device acquires 60 interference images at a sequence of wavelengths and least-square fits the first-order terms to calculate surface and optical thickness profiles.

A variation on this technique has been implemented by Deck,[19] in which a Fourier analysis of the interference spectrum extracts the frequencies and phases of all of the surfaces in a transparent flat. Zygo Corporation (Middlefield, CT) has successfully implemented this wavelength-tuned Fourier transform PSI in a commercial product that can measure both the front- and back-surface profiles, optical thickness variation, and index homogeneity.

1.1.4 Spatial separation of reflections

A grazing incidence interferometer by Dewa and Kulawiec[13] exploits the reflective surface properties of plane-parallel plates to individually measure surface topologies of either or both parallel surfaces of such test parts in a single mounting position. Illumination at the grazing incidence laterally shears reflections of a test beam from the two surfaces, and spatial coherence of an extended light

source is limited in relation to the lateral shear to prevent the formation of an undesired interference fringe pattern between the two parallel surfaces of the plate. In addition, this device provides for realigning a reference beam with the portion of the test beam that is reflected from one of the parallel surfaces, but not the portion that is reflected from the other surface. The realignment favors the formation of an interference fringe pattern between the reference surface and the one parallel test surface, to the exclusion of a similar interference pattern between the same reference surface and the other parallel test surface. This technique can be utilized to make the sheet appear thicker (i.e., longer than the illumination coherence length) for conventional PSI, or the reflections can be spatially separated for the front and back reflection using a relatively small scanning source.

Evans et al.[12] has also pursued a method of spatial separation of the two reflections. In this work, a Ritchey-Common configuration allows testing of flats with a spherical wavefront. With the flat at an angle to the expanding spherical wave propagation direction, a spatial shift in the two surface reflections occurs. This shift is a function of the thickness of the plate and the tilt angle. Additionally, rays reflected from the rear surface will be refracted as they traverse the front surface, producing an aberrated wavefront with focus displaced from the ideal position. Simulation and experimentation has demonstrated that this back reflection can be effectively spatially blocked with a stop.

Our application would certainly extend these techniques to their limit. Precise optical alignment will be paramount. The grazing incidence technique will also require precision machine design for a translating source and sensor. Linear and angular errors will directly affect the measurement accuracy.

1.1.5 Grating interferometry

An adjustable coherence depth interferometer has been studied by de Groot, Deck, and Lega.[14,15] This geometrically desensitized interferometer (GDI) uses two beams at different incident angles to generate an interference pattern with an equivalent wavelength of 5 to 20 μm. Recognizing that the coherence depth is a function of the size and shape of the light source, the GDI can separate the front and back reflections of transparent flats if the coherence depth is less than the sample thickness. In this work, the minimum coherence length obtained is 152 μm. This is just less than half of the 400-μm sample thickness for our work, so this technique may be feasible, although back fringes will be observable, yet attenuated. From the data reported,[15] the back reflection for our samples would be about 13 times weaker than the front.

1.1.6 Multimode laser diode

A Fizeau interferometer that utilizes a multilongitudinal-mode laser as a light source for testing transparent thin-plate samples has been developed by Ai.[16] As a result of the multimode laser operation, interference fringes are obtained only when the optical separation between the reference and test surfaces is an integer multiple of the laser's effective cavity length. By judicially selecting the multimode spectrum of operation and the effective cavity length of the laser, the interferometer may be calibrated to produce inter-

ference fringes at a workable optical separation between the reference and test surfaces, without ghost fringes from the opposite surface of the thin-plate sample.

For this technology to work in our application, there would need to be a sufficiently large number of modes under the gain curve in the power spectrum, so that the spikes in the coherence function would be very narrow. According to Ai,[16] the spike width, ~ 0.15 mm, was shorter than the glass thickness of 1 mm in his work, so there was no interference pattern between the sample's two surfaces.

1.1.7 Contact metrology

A contact metrology method was also considered. In this scheme, a touch probe that uses a high-frequency resonating stylus to detect contact with a test object would be used as a displacement transducer in an application similar to what is found in many contact coordinate measurement machines (CMMs). The probe requires 0.1 mN of force to detect contact. Application of this force to the center of a simply supported sheet without considering gravity would result in a deflection of

$$\delta_{\max} = \frac{PL^3}{48EI}, \qquad (1)$$

where the load $P = 0.1$ mN, foil optic length $L = 140$ mm, the modulus of elasticity for borosilicate glass $E = 6.3 \times 10^{10}$ N/m^2, and the moment of inertia I is further defined as

$$I = \frac{wh^3}{12}, \qquad (2)$$

where the foil width $w = 100$ mm and its thickness $h = 0.4$ mm. The resulting maximum deflection is $\delta_{\max} = 170$ nm. The small distortion is below the flatness tolerance. However, this system would require a vertical, high-precision stage to map the foil topography. Also, throughput would be restricted by the serial scanning procedure.

1.1.8 Shack-Hartmann

The Shack-Hartmann technology was developed by Platt and Shack[20] as an improvement to the existing Hartmann concept. Shack-Hartmann sensors do not rely on light-interference effects, but rather infer local near-field wavefront gradients by measuring a corresponding focused spot position in the far field. To do this, an array of lenslets is placed at the system image plane. This array dissects the incoming wavefront, as shown in Fig. 1. Each lenslet focuses its portion of the wavefront onto the charge coupled-device (CCD) detector array. The average wavefront tilt across each lenslet aperture results in a shift of the respective focal spot. A planar wavefront produces a regular array of focal spots, while an aberrated wavefront produces a distorted spot pattern. Comparing these two produces a map of the wavefront slopes, and integration of these slopes allows reconstruction of the test wavefront.[2,20] The wavefront incident on the lenslet array can be the test wavefront directly (i.e., 1:1 magnification) or it can be demagnified, as long as this is accounted for in the wavefront reconstruction software.
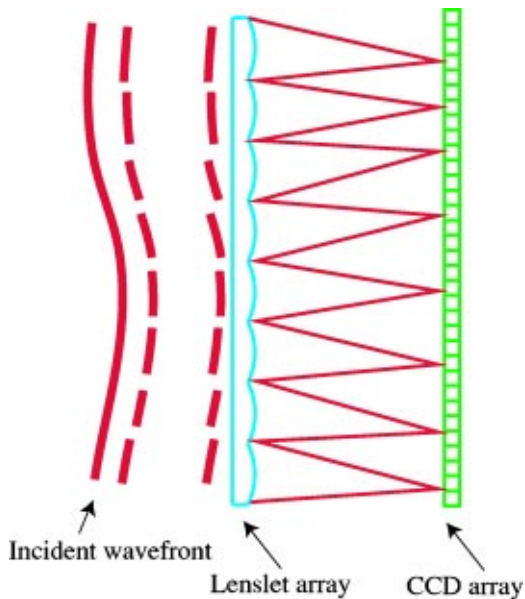
Fig. 1 Shack-Hartmann wavefront sensing concept.

1.2 *Justification for Shack-Hartmann Technology Selection*

The Shack-Hartmann technology offers a number of advantages over phase-shifting interferometry for our relatively large-optics metrology application. In the Shack-Hartmann system, temporally incoherent light sources can be used, which are generally cheaper than lasers. The sensors can produce short-duration frames either by shuttering the detector or by using a pulsed light source, thus mitigating the effects of vibrations and turbulence by allowing many effectively instantaneous measurements to be averaged.[21] Shack-Hartmann sensors can function in poorly controlled environments, such as a clean room with air turbulence and acoustic noise, that would introduce errors in phase-shifting interferometry measurements or preclude them

entirely.[22–24] The sensors themselves are much less complex and expensive than sequential PSIs and can provide greater angular dynamic range.

There are, of course, some drawbacks to this selection. The advantages are balanced by a reliance on the fidelity of the wavefront reconstruction algorithm, and by low spatial resolution and sensitivity as compared to PSI. According to a study by Koch et al.,[21] Shack-Hartmann sensors can measure difference wavefronts with a fidelity approaching that of a PSI, provided an appropriate number of individual measurements are averaged, and spatial resolution must be adequate for the application. This is especially true in our large optic application, where longer scale-length aberrations (e.g., due to mounting distortions) are important to characterize at full aperture, even with reduced angular sensitivity, but where high spatial frequency distortions can be measured more easily over small subapertures.

2 System Design Overview

The optical design for our deep-UV Shack Hartmann metrology tool is shown in Fig. 2. Collimated illumination is spectrally filtered and then focused by a beam expander lens. This light is then spatially filtered to propagate as an expanding spherical wave. The spherical wave is collimated by an off-axis paraboloid, which limits the maximum size of the object under test. The collimated light then reflects from the test optic, the paraboloid again, and the beamsplitter. The optical information is then recollimated by the relay lenses, dissected by a lenslet array inside the sensor, and falls onto a charge-coupled device (CCD) detector. From there, software interprets the image of the optic under test.

The layout is similar to a Keplerian telescope design, in that collimated input from the foil optic is demagnified to a collimated output to the wavefront sensor. Unwrapping this Keplerian portion of the metrology tool yields Fig. 3. The system magnification is accomplished using a large (200 mm diam) off-axis parabolic mirror in conjunction with relay lenses. The magnification of the system and the advantage of this layout can be derived from the system ma-
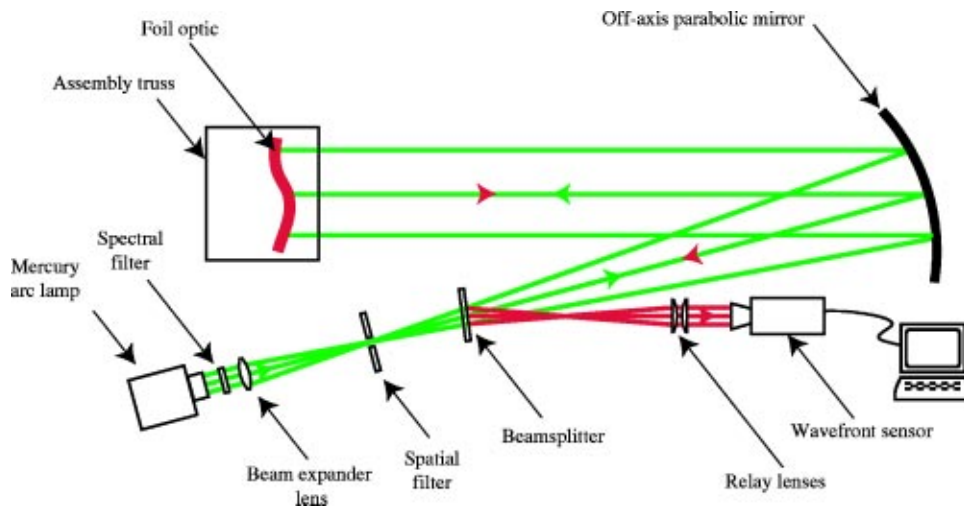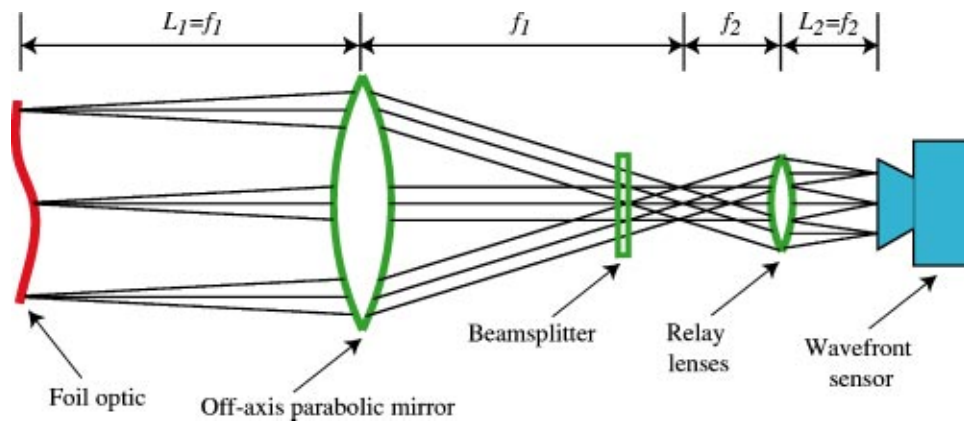

Fig. 2 Shack-Hartmann metrology tool.

Fig. 3 Portion of the Shack-Hartmann metrology system illustrating the intrinsic Keplerian design.

trix:

$$
\begin{bmatrix} A & B \\ C & D \end{bmatrix} = \overbrace{\begin{bmatrix} 1 & 0 \\ L_2 & 1 \end{bmatrix}}^{\text{Propagation to 2nd lens from sensor}} \underbrace{\begin{bmatrix} 1 & -\dfrac{1}{f_2} \\ 0 & 1 \end{bmatrix}}_{\text{Refraction from 2nd lens}}
$$

$$
\times \overbrace{\begin{bmatrix} 1 & 0 \\ f_1+f_2 & 1 \end{bmatrix}}^{\text{Propagation between lenses}} \underbrace{\begin{bmatrix} 1 & -\dfrac{1}{f_1} \\ 0 & 1 \end{bmatrix}}_{\text{Refraction from 1st lens}}
$$

$$
\times \overbrace{\begin{bmatrix} 1 & 0 \\ L_1 & 1 \end{bmatrix}}^{\text{Propagation to 1st lens from foil}} = \begin{bmatrix} \dfrac{1}{M} & 0 \\ 0 & M \end{bmatrix},
$$

(3)

where the first lens is replaced by the parabolic mirror and the second is the relay lens. Choosing $L_1=f_1=755.5$ mm and $L_2=f_2=75.0$ mm, the system magnification M, given by matrix element D, reduces to $-f_2/f_1=0.1$. The system has no effective optical power, as indicated by the B element. Element C shows that the effective propagation distance is zero—the effects of diffraction are minimized at the image plane. The system matrix is diagonal, revealing that position and tilt are decoupled.

3 Detailed Design

3.1 Arc Lamp

To provide the illumination for this optical metrology system, a 200-W broadband mercury arc lamp was selected. The photon emission is concentrated at the cathode and anode of the lamp, so-called hot-spots. A hot-spot can then be imaged onto a pinhole.

In operation, the nearly omnidirectional output of the lamp is amplified by a spherical rear reflector. The light then expands from the center of the lamp to fill a collimating lens located inside the arc lamp housing. After passing through the spectral filter, the light is focused by a positive power lens with an f number matched to the off-axis pa-

rabola. At the focus of this lens, a magnified image of the lamp is formed. The magnification is given by the ratio of the f numbers of the lenses as

$$
\text{arc magnification} = \frac{f/\#_2}{f/\#_1} = \frac{3.8}{1.5}, \tag{4}
$$

where $f/\#_1$ is for the collimating lens and $f/\#_2$ is for the beam expander lens. The original arc size of 0.6×2.2 mm^2 is therefore imaged to 1.5×5.7 mm^2. High spherical abberation will roughly double this image size, resulting in a 3×10 mm^2 arc image. This image is then spatially filtered, as shown in Fig. 2.

A 266-nm pulsed laser was considered for this application as well. The idea was rejected due to well-known problems of high peak power per pulse in a small beam waist, which could cause a breakdown in the air. However, the obvious benefits of higher power may require a revisitation of this issue in the future.

3.1.1 Arc instability

A major drawback to the arc lamp as a source is arc instability. Although the illumination from the electrodes shows good rotational symmetry,[25] there are spatial variations that can be detected by the wavefront sensor. These changes in local tilt and intensity are caused by convection currents inside the lamp, arc migration on the electrodes, and ambient temperature changes. Assuming these fluctuations are random with a Gaussian probability distribution, the effects
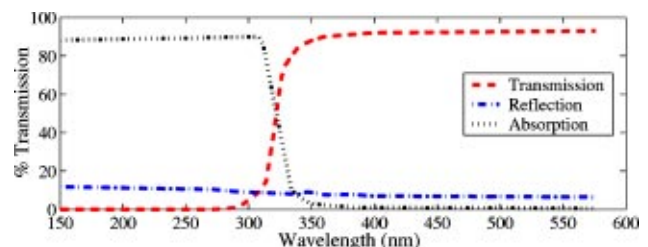

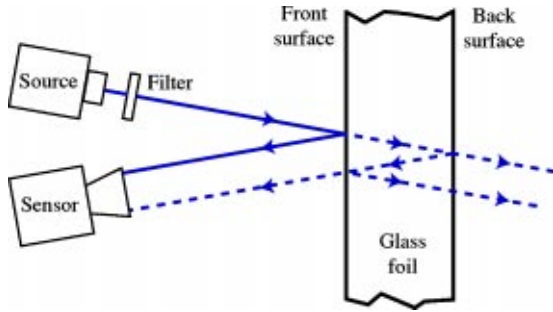**Fig. 4** Optical properties of 0.4-mm-thick borosilicate glass (Schott Glas, model D-263).

Fig. 5 Path of light reflected from front and back surfaces of glass into the sensor. Back reflections (*dashed line*) should be avoided.

Table 1 Comparison of spectral filters for Shack-Hartmann metrology system. The total power from the front reflection returned to the sensor is shown, along with the ratio of the power from the front and back reflection, named the focal spot intensity ratio.

Spectral filter peak λ (nm)	254	254	210	220	227
Filter shape	narrow	wide	broad	broad	broad
Power into sensor (μW)	1.1	4.1	7.2	9.5	7.8
Focal spot intensity ratio	>1000	40.0	3.9	4.6	5.5

on the metrology measurements have been mitigated by averaging 100 successive images over a two minute time span.

3.2 Spectral Filter

The optical properties of borosilicate glass (Schott Glas, model D-263) are shown in Fig. 4.[26] From the transmission curve, light incident on the glass foil at wavelengths greater than 300 nm will partially transmit through the substrate and reflect off its back surface. This will result in a doubled set of input data to the wavefront sensor (see Fig. 5), corrupting wavefront reconstruction. For example, if a longer wavelength HeNe laser were used for illumination, the ratio of the power from the front to back reflection would be 1.3. This would make the wavefront reconstruction erroneous. Therefore, we ideally seek a filter that passes 100% of the electromagnetic radiation below 260 nm and blocks 100% above. Of course, real filters simply attenuate all wavelengths to varying extents. We therefore need to balance the attenuation of the visible wavelengths and the total power input to the system. Filters considered are shown in Fig. 6.[27,28] As a baseline for the power measurements, the most conservative filter was installed in the system. Although this filter successfully blocked nearly all of the long wavelength light, only 1.1 μW of power was incident on the sensor. This resulted in a very low signal-to-noise ratio (SNR) with high gain. From this test, it was estimated that a signal strength increase of five times would be desirable.

To choose the best spectral filter from the options in Fig. 6, a simulation was created to evaluate 1. the total power incident on the detector, and 2. the power incident on the detector from the front and back reflections. This algorithm multiplies the lamp spectral irradiance by the filter trans-
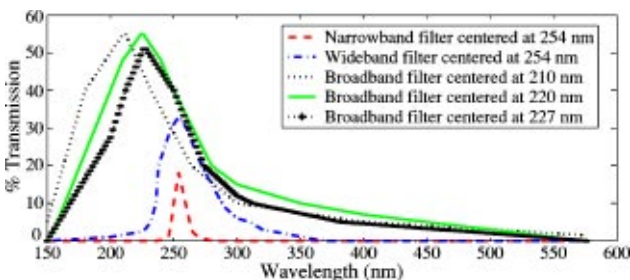
mission curve to calculate the spectra incident on the glass optic under test. Then, accounting for the transmission, reflection, and absorptive properties of the 0.4-mm-thick glass at the incident wavelengths, the spectra returned to the wavefront sensor from the front and back surface is computed. The lumigen-coated CCD responsivity is not constant over the wavelength band,[29] so this quantum efficiency is considered in the simulation as well. Integrating the resulting spectra yields the total powers returned from the respective reflections. These values indicate the relative intensity of the front and back focal spots on the detector. From this data, Table 1 was generated. For the 254-nm wideband filter, a plot of the front and back reflected power into the sensor is shown in Fig. 7. The ratio of the area under the front reflection curve to the area under the back reflection curve is 40.0, as confirmed in Table 1 for this filter. The back reflection power is below the sensor noise floor, making the error signal negligible. Also, the 4.1-μW total power incident on the CCD for the 254-nm wideband filter was satisfactory. For these reasons, this filter was selected.

3.3 Spatial Filter

The spatial filter has two functions. It cleans up the illumination from the arc lamp, reshaping the profile to an expanding spherical wave. The spatial filter also plays a key role in determining a lenslet's focal spot size on the detector. If the former were the sole factor, one would select the smallest pinhole that admitted power above a SNR threshold. However, the latter role of the spatial filter constrains the lower bound on the diameter.

Making the pinhole too large would do more harm than affecting the spherical wave profile. A large pinhole would effectively consume the dynamic range of the sensor, since
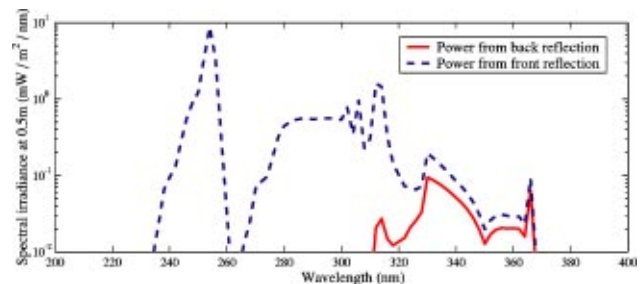

Fig. 6 Transmission curves for a range of spectral filters (Acton Research, Omega Optical).

Fig. 7 Irradiance reflected from glass sheets into wavefront sensors as a function of wavelength for the 254-nm wideband filter. This simulation considers the arc lamp spectral output, spectral filter transmission, optical properties of the borosilicate glass, and lumigen coating on the CCD.
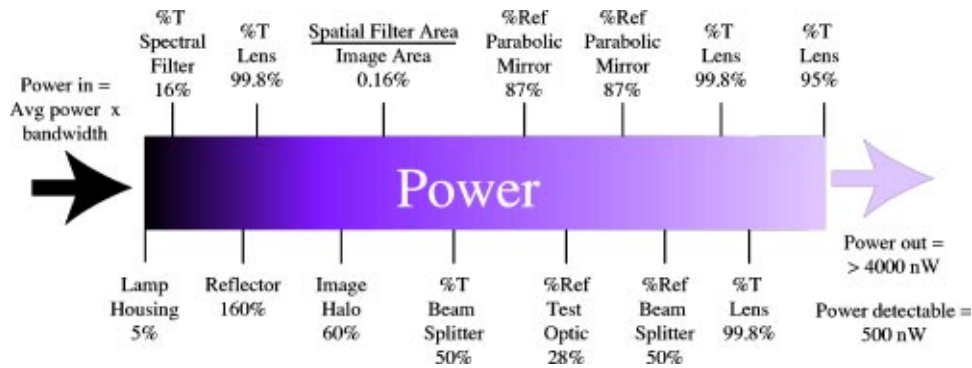
Fig. 8 Power losses throughout the optical path of the Shack-Hartmann surface metrology system.

a lenslet's focal spot would then cover all of the pixels dedicated to it. An upper bound on the pinhole size is thus imposed, such that the size of the focal spot on the detector should not exceed half of that lenslet's pixels. For the sensor selected, there are 16 pixels/lenslet.

To determine the size range for the pinhole, a few calculations need to be performed. A focal spot on the detector should cover at least 10 pixels for accurate centroiding, so the diameter of the spot should therefore be at least 3.6 pixels. Diffraction effects from the lenslet array will increase the focal spot size. A collimated input to a lenslet will have a focal spot diameter due to diffraction, given by

$$d_{\text{focal spot, diffraction only}} = \frac{2\lambda f_{\text{lenslet}}}{d_{\text{lenslet}}}. \tag{5}$$

Using the peak transmitted wavelength λ of 253.7 nm, the lenslet parameters diameter d_{lenslet} of 224 μm, and the focal length at λ, f_{lenslet}, of 17.904 mm, the focal spot diameter due to diffraction is 40.6 μm.

Next, we need to consider the demagnified pinhole contribution. This demagnification is given by the ratio of the focal lengths of the lenslet array and the relay optic. The other lenses do not contribute to the demagnification since a conjugate 1:1 magnification of the pinhole occurs between the beamsplitter and the relay lenses, as shown Fig. 2. Therefore, the diameter of the pinhole image on the detector is given by

$$d_{\text{pinhole image}} = \frac{f_{\text{lenslet}}}{f_{\text{relay optic}}} d_{\text{pinhole}}. \tag{6}$$

With f_{lenslet} given before and $f_{\text{relay optic}} = 75.0$ mm, the pinhole diameter on the CCD is 0.239 d_{lenslet}. Hereafter, m will denote the pinhole magnification of 0.239.

These two effects, diffraction and pinhole demagnification, are combined by convolution. This is approximately the same as addition in this case, yielding a total focal spot size on the detector of 40.6 μm + 0.239d_{pinhole}. This focal spot diameter must cover at least 3.6 pixels for sensitivity, as previously mentioned, but not more than $(1/2)16 = 8$ pixels for dynamic range. Since the pixel size is 14 μm, we have

$$3.6 \text{ pixels} < \frac{40.6 \ \mu\text{m} + (0.239)(d_{\text{pinhole}})}{14 \ \mu\text{m/pixel}} < 8 \text{ pixels.} \tag{7}$$

To satisfy this inequality, the pinhole diameter must be between 41 and 299 μm in size. To admit as much power as possible, a 250-μm-diam pinhole was selected.

3.4 Power Considerations

Making sure that enough irradiance would reflect from the inefficient glass and return to the sensor for a successful measurement was a prime consideration in the design. Irradiance from the source is lost at many locations along the optical path, as illustrated in Fig. 8. To keep track of the power remaining for imaging, we need to calculate the power into the system and the power lost. This process starts with the arc lamp inside of the lamp housing. To find the total power coming out of this lamp, the spectral filter bandwidth (FWHM) is multiplied by the average power from the lamp spectral irradiance curve over this bandwidth. From Fig. 6, the FWHM is 40 nm. The average flux from the lamp over this bandwidth is 35 mW/m^2-nm.[25] So the flux from the lamp is 1400 mW/m^2.

Three multiplicative factors next affect this power: the spectral filter transmittance, lamp housing rear reflector, and the housing itself. The filter transmittance at FWHM is approximately 20%, again obtained from Fig. 6. The lamp housing rear reflector acts as an amplifier, yielding a 160% boost.[25] The housing itself is naturally very lossy, since the omnidirectional irradiance is mostly wasted, excluding the contribution from the rear reflector. The housing factor is a mere 5%.[25] So in the exit tube of the lamp housing, we have 1400 mW/m$^2 \times 0.2 \times 1.6 \times 0.05 = 22.4$ mW/m^2.

The antireflection-coated fused-silica beam-expander lens at the end of the condenser (exit tube) transmits 99.8% of incident light. So the image of the arc formed at the spatial filter contains 22.4 mW $\times 0.998 = 22.34$ mW/m^2. As mentioned in Sec. 3.1, this image size is 30 mm^2. About 40% of this power is lost in a "halo" around the image, further reducing our available power to 13.4 mW. Next, we spatially filter with a 250-μm pinhole, as described in Sec. 3.3. The ratio of the area of this pinhole to the area of the image is 0.16%, so a mere 21 μW makes it through.

This light then goes through a veritable pinball machine of mirrors and lenses until it is incident on the CCD detec-

Table 2 Optical element transmission (T) and reflection (R) percentages from spatial filter to CCD detector. The items are listed in the order that the light "sees" them. Repeated items are seen twice. High transmission percentages are due to antireflection coatings.

Optical element	T,R	%	Reference
Beamsplitter	T	50	30
Parabola	R	87	31
Test optic (Si or glass)	R	50	32
Parabola	R	87	31
Beamsplitter	R	50	30
Relay optic 1	T	99.8	33
Relay optic 2	T	99.8	33
Lenslet array	T	95	34
Total		15.6	

Table 3 Wavefront sensor lenslet array, detector, and system magnification summary.

System			
Operating wavelength	λ	254 nm	
System magnification	M	-0.1	
Pinhole magnification	m	0.239	
Pinhole diameter	d_p	250 μm	
Lenslet			
Lenslet diameter	d_l	0.224 mm	
Lenslet focal length at λ	f_l	17.904 mm	
Nominal sag		1.378 μm	
Active number of lenslets X	N_l	64	
Active number of lenslets Y	N_l	64	
Total number of lenslets X		72	
Total number of lenslets Y		72	
Total aperture X	D	16.128 mm	
Total aperture Y	D	16.128 mm	
Detector			
Pixel size X	p	14 μm	
Pixel size Y	p	14 μm	
Number of pixels X	N_p	1024	
Number of pixels Y	N_p	1024	

tor inside of the wavefront sensor. The percentage transmitted or reflected by each component in normal operation is summarized in Table 2.[30–34] These data were compiled from intensity graphs as cited. Intensity data can be used since power is proportional to intensity. So the final power incident on the CCD detector is 21 μW from the spatial filter multiplied by 15.6% for the optical elements downstream. This theoretical calculation gives roughly 3.3 μW of power centered at 254 nm to excite electrons in the CCD. This light is then divided unevenly by the lenslets over the 1024×1024-pixel CCD. Is this enough? Tests of the measurable power threshold for this instrument indicate that 500 nW is detectable, but 1 μW is needed for a lower gain, higher SNR measurement. An experimentally incident power of 4.1 μW, as shown in Table 1, is therefore satisfactory. There is good agreement between the theoretically calculated power of 3.3 μW and the measured 4.1 μW.

3.5 Wavefront Sensor

There were a number of tradeoffs considered in the selection of this device, as identified by Greivenkamp et al.[2] The spot displacement on the detector is equal to the wavefront slope times the focal length of the lenslet. A limitation to the maximum allowable wavefront slope, or dynamic range, is imposed by the detector area allocated to that lenslet. This is primarily a software-based limitation. There is no inherent requirement that a spot remain within the cell of pixels associated with its lenslet. Spots can translate several cells as long as the one-to-one correspondence between the spots and the lenslets can be mapped or identified.[2] For the same detector, a lenslet array with a shorter focal length will have greater dynamic range with reduced sensitivity. On the other hand, a longer focal length lenslet will allow greater accuracy in determining the average incident wavefront slope, since a given slope produces a greater spot displacement. So there is a tradeoff of sensitivity and dynamic range associated with the lenslet focal length.

The size versus number of lenslets is another important tradeoff. As the number of lenslets is increased for a given area, spatial sampling and spatial resolution are increased. This results in less averaging of the wavefront slope over the lenslet aperture, but reduces the number of detector pixels that are available behind each lenslet to make the

measurement. Selecting larger lenslets will allow a more sensitive measurement of slowly varying wavefronts, but may not sufficiently sample high spatial frequency wavefronts, producing artificially smooth surface maps.

Pixel size on the detector and the lenslet f number are also related. The spot size produced by each lenslet must be sufficiently large (covering at least 10 pixels in area) to obtain a good centroid calculation, while separation between spots from adjacent lenslets must be maintained to ensure dynamic range. As a general rule, the spot size diameter should not cover more than half of the number of pixels dedicated to a lenslet's diameter for a reasonable balance of sensitivity and dynamic range. The spot size scales linearly with the wavelength and lenslet f number, so the lenslet diameter and focal length should be selected wisely.

3.5.1 SMD 1M15 instrument

Wavefront Sciences (Albuquerque, New Mexico) provided the SMD 1M15 wavefront sensor for our application.[35] The instrument features a 64×64 lithographically etched, fused silica lenslet array. Table 3 displays a summary of the notable physical characteristics of the instrument's lenslet array and detector, along with some system magnifications. The CCD detector was coated with lumigen by Spectral Instruments[36] (Tucson, Arizona) to increase its quantum efficiency. The lumigen coating is 30 to 40% efficient in absorbing the incident light at 250 nm and up-converting to 500 nm. (The lumigen coating is actually 60 to 80% efficient in absorbing the incident light at 250 nm and up-converting to 500 nm. However, the lumigen is a thin layer on top of the CCD, so half of the photons are emitted in each direction, thus you lose 50% is lost from the directionality). In selecting this unit, its ability to meet our func-
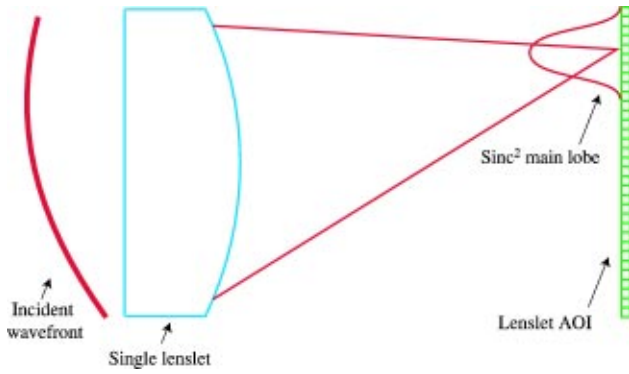
Fig. 9 The high tilt of the incident wavefront results in a focal spot shift to the edge of the lenslet's AOI. This is the extent of the instrument's angular range.

tional requirements for sensitivity and dynamic angular range were paramount. These goals, described in Sec. 1, are 10 μrad and 0.3 mrad, respectively.

The dynamic range of measurement is limited by the detector area allocated to each lenslet (named the area-of-interest or AOI). When the focal spot behind a lenslet encroaches on the edge of its AOI, crosstalk occurs and wavefront reconstruction is compromised. This limitation to focal spot shift is depicted in Fig. 9. The angular range for this instrument can be geometrically estimated from the lenslet diameter of 0.224 mm and operating focal length of 17.904 mm to be approximately ± 6 mrad. Taking the system magnification into account allows one to estimate the measurable dynamic range at the object plane to be $|-0.1 \times 6 \text{ mrad}| = 0.6$ mrad. To make a more accurate calculation, we need to consider the focal spot size. The focal spot radius on the CCD at the 254-nm operating wavelength, $r_{\text{spot},254}$, is given by

$$r_{\text{spot},254} = \frac{f_l \lambda}{d_l} + \frac{m d_p}{2}. \tag{8}$$

From the values in Table 3, the spot size is 50.2 μm. This will effectively reduce the lenslet diameter. So the actual dynamic range, considering the magnification, will be

$$\text{dynamic range} = M \left[\frac{\left(\frac{d_l}{2} - r_{\text{spot},254} \right)}{f_l} \right], \tag{9}$$

which gives a value of 0.35 mrad. This instrument will therefore meet the dynamic range requirement of 0.3 mrad at the object plane. This angular range is the same for one lenslet or the set of lenslets. For one lenslet with a diameter of 224 μm, which corresponds to 2.24 mm at the object plane, a wavefront tilt of 0.78 μm can be measured. Since $N_l = 64$, the maximum measurable object tilt over the entire lenslet array is 0.78 μm $\times 64 = 50.18$ μm over a 143.3-mm lateral distance.

Estimating the instrument's sensitivity is a bit more difficult. We need to calculate the noise floor after algorithmic wavefront reconstruction. This analysis requires experimental data for the centroid estimation error as well as

knowledge about the digital signal processing used for numerical reconstruction of the wavefront shape. We start off by calculating the centroid estimation error at the operating wavelength, e_{254}. As a baseline, the manufacturer has tested the centroid estimation error for a similar instrument at 633 nm, yielding $e_{633} = 0.0025$ pixels. To extrapolate our estimate, we need to scale by the square of the diffraction-limited spot half widths at this baseline wavelength and the operating wavelength. The square is used to realize an area contribution from a length measurement.

$$e_{254} = e_{633} \left[\frac{\dfrac{f_l(254 \text{ nm})}{d_l}}{\dfrac{f_b(633 \text{ nm})}{d_b}} \right]^2. \tag{10}$$

For the baseline sensor tested at 633 nm, f_b and d_b are its lenslet focal length and diameter, respectively, which gives $f_b(633 \text{ nm})/d_b = 36.0$ μm. The resulting $e_{254} = 0.0079$ pixels. Now we must use this information to calculate our instrument's rms angular noise floor. This is a function of the angle to the edge of a pixel and centroid estimation error. Including the magnification will translate us to the object plane. The noise floor is therefore

$$\theta_{\text{rms}} = M \left(\frac{p e_{254}}{f_l} \right), \tag{11}$$

resulting in $\theta_{\text{rms}} = 0.61$ μrad. The minimum measurable variation from flatness, or noise floor, is influenced by the numerical reconstruction algorithm as follows:

$$\text{noise floor} = \sqrt{N_l} d \theta_{\text{rms}}. \tag{12}$$

The lenslet diameter is included to compute the "per lenslet" noise floor. A factor of the square root of the number of lenslets is introduced to effectively account for the error's random walk over the lenslet array. Equation (12) therefore gives the final numerically reconstructed noise floor, PV. This minimum measurable deviation from flatness is equal to 1.1 nm. This could occur over a lateral distance as short as 2.24 mm (one lenslet's diameter magnified). So, this sensitivity corresponds to an angular resolution of 0.5 μrad for one lenslet. As greater lateral distances are considered, the angular resolution improves, so the sensitivity functional requirement of 10 μrad is always met.

Comparing these calculated values back to the functional requirements, for a 10-mm lateral distance in the object plane, we have theoretically measurable PV height of ± 3.5 μm with a resolution of ± 1 nm.

4 Performance Evaluation

4.1 Test Optic Surface Mapping

The Shack-Hartmann surface metrology instrument, shown in Fig. 10, has been successfully used to generate surface maps of large $\lambda/30$ reference flats, 0.45-mm-thick $\times 100$-mm-diam polished silicon wafers as are commonly used in semiconductor industry, and $100 \times 140 \times 0.4$-mm^3 glass sheets. The system can provide both angular devia-
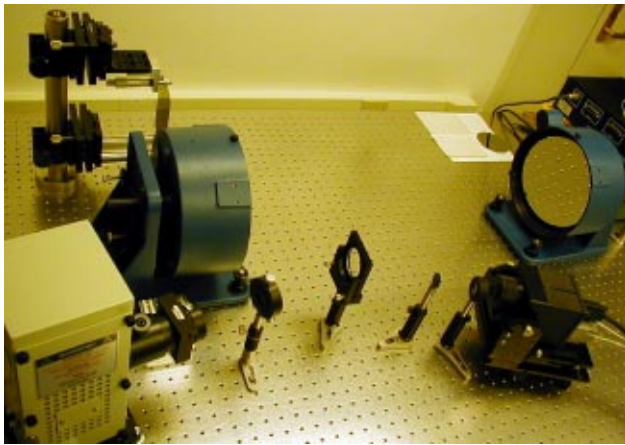
Fig. 10 Shack-Hartmann metrology system hardware in a class 1000 cleanroom environment at the MIT Space Nanotechnology Laboratory.

tions from flatness and absolute PV measurements. The former are critical to telescope resolution, while the latter are of immediate use in polishing and shaping.

Measurement of a 0.4-mm-thick borosilicate glass sheet is shown in Fig. 11. Results from glass metrology show no indication of back reflections in the raw data. The array of focal spots is regular and the frequency of spots is as expected, one per AOI. Large warp in prefigured stock glass sheets makes their entire surface unmeasurable; however, subset regions have been successfully measured.

4.2 *Repeatability and Accuracy*

The repeatability of the measurements has been primarily limited by random variations in the arc lamp caused by arc migration on the electrodes and convection currents inside the lamp.[25] Averaging 100 successive images has mitigated the effects of these variations, reducing the range of PV surface maps to 5.0 nm rms) over a minimum 100-mm-diam object size while the setup is unchanged. To determine the repeatability of the instrument for a human-in-the-

loop environment, specimens were measured, physically removed from the metrology station, replaced, and remeasured. Both the reference surface and the silicon wafer specimens were studied; results were similar. Repeatability measurements ranged 35.6-nm PV with a 13.2-nm standard deviation. The rms surface variations ranged 14.0 nm with a 5.1-nm standard deviation.

The accuracy of the system is difficult to quantify, since aberrations in the lenses will contribute different angular errors to measurements at different spatial locations. To roughly estimate the overall accuracy of the system, two flats with factory-provided interferograms were measured. These interferograms reveal nonflatnesses of 2.6-nm rms and 4.9-nm rms, respectively. Comparing the two flats with the Shack-Hartmann system shows an average rms surface difference of 17.6 nm. Overlapping the interferograms, the rms deviation can be estimated to be $\sqrt{2.6^2+4.9^2}$ $=5.5$ nm. The difference between the Shack-Hartmann and interferometric data provides a crude estimation of the accuracy of the tool. Assuming root-sum-squared (RSS) stacking of errors, a conservative estimate of the accuracy yields $\sqrt{17.6^2-5.5^2}=16.7$-nm rms. Several factors contribute to the difference between the interferograms and Shack-Hartmann measurements. The mirrors are subjected to different temperatures and mounting forces between the instruments. Additionally, the uncertainty in the interferometric measurements is estimated to be $\lambda/50\approx13$-nm PV.

In operation, the user will make a reference image with a flat, then substitute the optic under test. Based on the earlier analysis, the test measurement will be accurate to <17 nm and repeatable to ~5 nm rms. These results are summarized in Table 4.

5 Conclusions

A Shack-Hartmann surface metrology tool is developed that permits metrological feedback of transparent or opaque optic foils. This instrument can be used to determine if a surface meets the 500-nm global flatness manufacturing requirement. The surface mapping data is accurate to <17-nm and repeatable to ~5 nm rms. Nonflat figures can

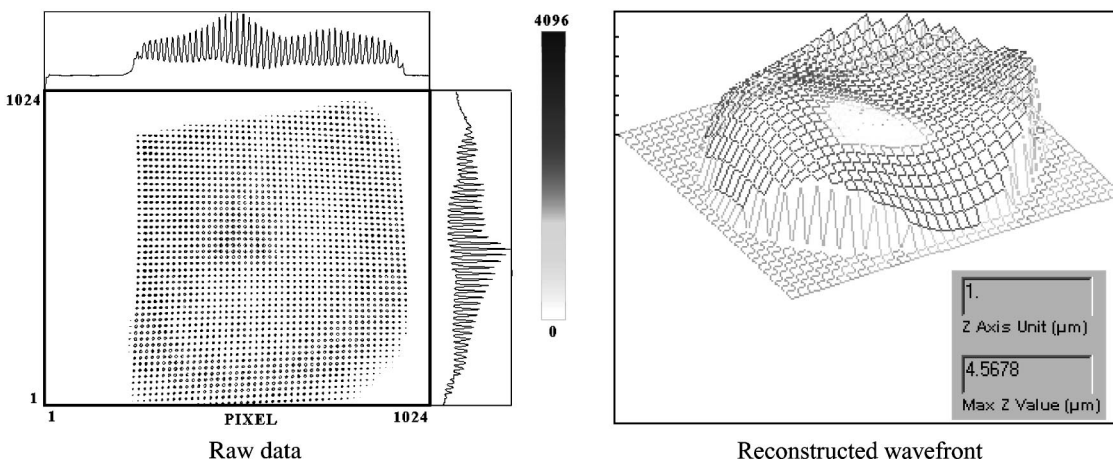|	
Raw data	Reconstructed wavefront

Fig. 11 Raw data (*left*) is collected on the CCD array in the wavefront sensor. Comparison with a reference image, regular array focal spots from a λ/30 flat mirror, enable the wavefront reconstruction (*right*), which is equivalent to a surface map at the object plane. The intensity scale (*center*) indicates the relative energy density incident on the CCD in $2^{12}=4096$ discrete values.

Table 4 Shack-Hartmann surface metrology system performance results.

Setup	Statistic	PV (nm)	rms (nm)
Static			
Repeated	Range	5.0	0.5
measurements			
Repeatability	Range	35.6	14.0
Removed and			
replaced object	Standard deviation	13.2	5.1
Accuracy			
Compared two	Average	-	<16.7
known surfaces			

also be studied up to a dynamic range of $\pm 350\ \mu$rad at the object plane. The 143×143-mm^2 square viewing range can accommodate the proposed 140×100-mm^2 foil optic surface area.

Acknowledgments

References

1. C. R. Forest, M. L. Schattenburg, C. G. Chen, R. K. Heilmann, P. Konkola, J. Przbylowski, Y. Sun, J. You, S. M. Kahn, and D. Golini, "Precision shaping, assembly and metrology of foil optics for x-ray reflection gratings," *Proc. SPIE* **4851**, 538–548 (2002).
2. J. E. Greivenkamp, D. G. Smith, R. O. Gappinger, and G. A. Williby, "Optical testing using Shack-Hartmann wavefront sensors," *Proc. SPIE* **4416**, 260–263 (2001).
3. ADE Phase-Shift. 3470 E. Universal Way, Tucson, AZ 85706.
4. J. Schwider, "White-light fizeau interferometer," *Appl. Opt.* **36**, 1433–1437 (Mar. 1997).
5. K. Takada, I. Yokohama, K. Chida, and J. Noda, "New measurement system for fault location in optical waveguide devices based on an interferometric technique," *Appl. Opt.* **26**, 1603–1606 (1987).
6. C. Hitzenberger, "Measurement of cornea thickness by low-coherence interferometry," *Appl. Opt.* **31**, 6637–6642 (1992).
7. R. Dandliker, E. Zimmermann, and G. Frosio, "Electronically scanned white-light interferometry: a novel noise-resistant signal processing," *Opt. Lett.* **17**, 679–681 (1992).
8. K. Okada and J. Tsujiuchi, "Wavelength scanning interferometry for the measurement of both surface shapes and refractive index inhomogeneity," *Proc. SPIE* **1162**, 395–401 (1989).
9. K. Okada, H. Sakuta, T. Ose, and J. Tsujiuchi, "Separate measurements of surface shapes and refractive index inhomogeneity of an optical element using tunable-source phase shifting interferometry," *Appl. Opt.* **29**, 3280–3285 (1990).
10. P. de Groot, "Measurement of transparent plates with wavelength-tuned phase-shifting interferometry," *Appl. Opt.* **39**, 2658–2663 (June 2000).
11. P. de Groot, R. Smythe, and L. Deck, "Laser diodes map surface flatness of complex parts," *Laser Focus World*, 95–98 (Feb. 1994).
12. C. J. Evans, R. E. Parks, L. Z. Shao, T. Schmitz, and A. Davies, "Interferometric testing of photomask substrate flatness," *Proc. SPIE* **4344**, 844–851 (2001).
13. P. G. Dewa and A. W. Kulawiec, "Grazing incidence interferometry for measuring transparent plane-parallel plates," U.S. Patent No. 5,923,425 (Jul. 1999).
14. P. de Groot, L. Deck, and X. C. de Lega, "Adjustable coherence depth in a geometrically-desensitized interferometer," *Proc. SPIE* **3479**, 14–23 (1998).
15. P. de Groot, "Grating interferometer for metrology of transparent flats," *Opt. Fabrication Testing* **6**, 28–30 (1996).
16. C. Ai, "Multimode laser fizeau interferometer for measuring the surface of a thin transparent plate," *Appl. Opt.* **36**, 8135–8138 (Nov. 1997).
17. R. K. Heilmann, G. P. Monnelly, O. Mongrard, N. Butler, C. G. Chen, L. M. Cohen, C. C. Cook, L. M. Goldman, P. T. Konkola, M. McGuirk, G. R. Ricker, and M. L. Schattenburg, "Novel methods for shaping thin-foil optics for x-ray astronomy," *Proc. SPIE* **4496**, 62–72 (2002).
18. G. Schulz, "Zweistrahlinterferenz in planspiegelanordnungen," *Opt. Acta* **11**, 43–60, 89–99, 131–143 (1964).
19. L. Deck, "Fourier-transform phase shifting interferometry," *Appl. Opt.* **42**, 2354–2365 (2003).
20. B. C. Platt and R. Shack, "History and principles of Shack-Hartmann wavefront sensing," *J. Refract. Surg.* **17**, 573–577 (2001).
21. J. A. Koch, R. W. Presta, R. A. Sacks, R. A. Zacharias, E. S. Bliss, M. J. Daily, M. Feldman, A. A. Grey, F. R. Holdener, J. T. Salmon, L. G. Seppala, J. S. Toeppen, L. V. Atta, B. M. V. Wonterghem, W. T. Whistler, S. E. Winters, and B. W. Woods, "Experimental comparison of a Shack-Hartmann sensor and a phase-shifting interferometer for large-optics metrology applications," *Appl. Opt.* **39**, 4540–4546 (Sep. 2000).
22. D. Malacara, *Optical Shop Testing*, 2nd ed., Wiley and Sons, New York (1992).
23. C. Koliopolis, "Simultaneous phase shift interferometer," *Proc. SPIE* **1531**, 119–127 (1991).
24. B. M. Welsh, B. L. Ellerbroek, M. C. Roggemann, and T. L. Pennington, "Fundamental performance comparison of a Hartmann and a shearing interferometer wavefront sensor," *Appl. Opt.* **34**, 4186–4195 (1995).
25. *The Book of Photon Tools*, Oriel Instruments, 150 Long Beach Blvd., Stratford, CT 06615 (2001).
26. SCHOTT Corporation, 3 Odell Plaza, Yonkers, NY 10701.
27. Acton Research Corporation, 15 Discovery Way, Acton, MA 01720.
28. Omega Optical, Inc., 210 Main Street, Brattleboro, VT 05301.
29. Seishin Trading Co., LTD., 2-1, 1-chome Sannomiya-cho, Chuo-ku, Kobe, 650-0021 Japan.
30. OptoSigma, 2001 Deere Avenue, Santa Ana, CA 92705.
31. Space Optics Research Labs., 7 Stuart Road, Chelmsford, MA 01824.
32. *Handbook of Optical Constants of Solids*, E. D. Palik, Ed., Academic Press, San Diego, CA (1985).
33. Lambda Research Optics, Inc., 1695 W. MacArthur Blvd., Costa Mesa, CA 92626.
34. JML Optical Industries, Inc., 690 Portland Avenue, Rochester, NY 14621.
35. WaveFront Sciences, Inc., 14810 Central Ave. SE, Albuquerque, NM 87123-3905.
36. Spectral Instruments, 420 North Bonita Avenue, Tucson, AZ 85745.

Craig R. Forest is currently a PhD candidate in the Department of Mechanical Engineering at the Massachusetts Institute of Technology in the research group of A. Slocum. He received a BS in mechanical engineering in 2001 from the Georgia Institute of Technology, and MS in mechanical engineering in 2003 from the Massachusetts Institute of Technology. His current research interests include MEMS, optics, and precision machine design. His recent research efforts have focused on providing metrology and assembly technology for NASA's next generation x-ray telescope, as well as optical MEMS sensors.

Claude R. Canizares is Associate Provost and the Bruno Rossi Professor of Experimental Physics at MIT and is a professor at the Center for Space Research. He is a principal investigator on NASA's Chandra X-ray Observatory, leading the development of the high resolution transmission grating spectrometer for this major space observatory, and is Associate Director of the Chandra X-Ray Observatory Center. He has also worked on several other space astronomy missions, including as coinvestigator on the Einstein Observatory (HEAO-2). His main research interests are high resolution spectroscopy and plasma diagnostics of supernova remnants and clusters of galaxies, cooling flows in galaxies and clusters, x-ray studies of dark matter, x-ray properties of quasars and active galactic nuclei, and gravitational lenses. He is a member of the Board of

Daniel R. Neal obtained his Bachelors of Science from the University of Texas in aerospace engineering in 1980, and his PhD from Stanford University in aeronautics and astronautics and applied physics in 1984. For 13 years he worked at Sandia National Laboratories developing high-energy laser systems. During that time, he developed numerous laser diagnostic instruments, adaptive optics, laser resonators, and micro-optics systems. He also designed a series of increasingly sophisticated instruments for measuring aberrations in lasers and optics. The early film-based Hartmann sensing evolved to a 1-D, all electronic Shack-Hartmann sensor, which was used for wind-tunnel, tomographic and hypersonic diagnostics and other applications. In 1995, in conjunction with business partner T. Turner, he founded WaveFront Sciences, Incorporated, to commercialize the Shack-Hartmann and micro-optics technologies. Since then, he has developed many different wavefront sensor configurations and instruments, including applications to optic, laser beam, silicon wafer, and ophthalmic testing.

Michael McGuirk: Biography and photograph not available.

Mark L. Schattenburg is a Principal Research Scientist in the MIT Center for Space Research. He is Director of the Space Nanotechnology Laboratory, Associate Director of the NanoStructures Laboratory and Senior Research Affiliate with the Microsystems Technology Laboratories. His principal work has been in the area of micro/nanofabrication technology, optical and x-ray interferometry, advanced lithography including x-ray and electron beam, nanometrology, x-ray optics and instrumentation, x-ray astronomy, high-resolution x-ray spectroscopy, and space physics instrumentation utilizing nanotechnology. He is a member of the NASA Chandra Science and Instrument Development Teams, the Constellation-X Facility Science Team, the Micro-Arcsecond X-Ray Imaging Mission (MAXIM) Study Team, and the NASA/ESA Laser Interferometer Space Antenna (LISA) Study Team. He is also a member of the steering committee of the International Conference on Electron, Ion and Photon Beam Technology and Nanofabrication, serving as program chair in 2003. He received a BS degree in physics from the University of Hawaii in 1978, and a PhD in physics from MIT in 1984. He was appointed postdoctoral associate at MIT in 1984, progressing to Principal Research Scientist in 1996. He has published more than 120 papers and holds six patents. He is a member of the Optical Society of America, the American Vacuum Society, DPIE, the Institute of Electrical and Electronic Engineers, and the American Society for Precision Engineering. He was awarded the 2003 BACUS Prize by SPIE.